50 Hz X-Ray Diffraction Stress Analysis and Numerical Process Simulation at Laser Surface Line Hardening of Web Structures

Dominik Kiefer,* Florian Lang, Nicola Simon, Felix Beckmann, Fabian Wilde, and Jens Gibmeier

In situ synchrotron X-ray diffraction experiments were carried out during laser surface line hardening of the common tempering steel AISI 4140 at beamline P05@PETRA III operated by Helmholtz-Zentrum Geesthacht at the Deutsches Elektronen Synchrotron, Hamburg, Germany. A unique process chamber was used to investigate the phase and transverse surface stress evolution during a laser line hardening processes. Synchrotron radiation, in combination with microstrip line detectors, allows for a time resolution of 50 Hz. Specimen geometries were hardened using a high-power diode laser under control of the surface temperature and constant laser beam feed. Herein, it is focused on web-structured specimens in contrast to a flat geometry. The experimental results are discussed with regard to the workpiece geometry effect of the web structure dimensions on the temporal and spatial stress evolution. In addition, numerical process simulations based on the finite element method were carried out to support the drawn conclusions. The presented model is able to predict the surface transverse stresses inside the process zone center, while providing further 3D information. A heat build-up in the web leads to a wider and deeper process zone, however, the absolute hardness increase and the transverse residual stresses at the surface center are not affected.

1. Introduction

The improvement of surface layers of structural steel components is of great importance in mechanical engineering, as failure for highly stressed technical components, as e.g., the formation of fatigue cracks or oxidization, initiates primarily at the very surfaces. Here, surface hardening heat treatments[1] provide a suitable tool to increase wear and fatigue strength. Among the multitude of surface hardening processes,[1] laser surface hardening became increasingly popular in the past few decades, even more so with the development of High-Power Diode Lasers (HPDL).[2–4] The process is characterized by the precise and local heating of a steel workpiece using a focused laser beam, thereby austenitizing the process zone, followed by rapid self-quenching through heat conduction into the surrounding cold material and hence martensitic hardening. This surface hardening is accompanied by the formation of favorable residual stress states, i.e., predominantly compressive stresses, inside the process zone. The advantages of laser surface hardening over other steel hardening processes are i) the minimal distortion due to the fast and precise heat input, ii) the omitted requirement for a secondary quenching medium, and therefore, a high and flexible automation capability, and iii) the reduced environmental impact due to a lower power consumption. A brief description and explanation of the laser hardening process was given by Ion.[5] A lot of research was already done on laser surface hardening, mostly focusing on the numerical process prediction of the hardening result, e.g., hardening depth, width, and degree.[6–10] Only minor interest was given to the formation of residual stresses induced by laser surface hardening. De la Cruz et al.,[11] for example, showed the positive effect of laser surface hardening on fatigue resistance in comparison with quenched and tempered material states due to the induced compressive residual stresses. In literature, there are multiple different numerical models which allow the prognosis of transient process stresses and resulting residual stresses, e.g., studies by Liverani et al., Müller et al., and Bailey et al.,[9,12,13] at low cost and effort. However, in our judgment, the transient process stress and residual stress prediction by

D. Kiefer, F. Lang, N. Simon, Dr. J. Gibmeier
Institute for Applied Materials (IAM-WK)
Karlsruhe Institute of Technology (KIT)
Engelbert-Arnold-Str. 4, Karlsruhe 76131, Germany
E-mail: Dominik.Kiefer@kit.edu

Dr. F. Beckmann, Dr. F. Wilde
Institute of Materials Physics
Helmholtz-Zentrum Geesthacht (HZG)
Max-Planck-Str. 1, Geesthacht 21502, Germany

The ORCID identification number(s) for the author(s) of this article can be found under https://doi.org/10.1002/adem.202100119.

**ADVANCED
SCIENCE NEWS**

www.advancedsciencenews.com

**ADVANCED
ENGINEERING
MATERIALS**

www.aem-journal.com

numerical simulations, in comparison with experimentally determined residual stresses, is currently insufficient, as in some cases, larger deviations between experiment and simulation occurred. For an improved process understanding, especially on the stress formation during laser surface hardening, cost, and time-intensive postprocess characterizations are inadequate. However, real-time data of phase transformation and stress evolution represent an advantage in this regard. Hence, this knowledge will certainly help facilitating numerical simulations and will enable process predictions on a quantitative level. The authors developed a unique experimental setup to investigate the temporal evolution of surface parallel stresses during the actual laser hardening process.[14–17] After beginning with static spot hardening in situ analysis,[14] further developments of the experimental setup lead to the more process-oriented[15,17] line hardening of flat and curved specimens. Based on previous results, in this study, we intend to investigate the effect of constrained heat conduction by comparing different web geometries with a flat specimen.

2. Experimental Section

2.1. Material, Sample Preparation, and Laser Hardening

The laser line hardening was carried out on steel AISI 4140 (1.7225) in a quenched and tempered state. The chemical composition of the material is determined by optical emission spectroscopy and shown in **Table 1**. Three different sample geometries were machined from blocks of AISI 4140. One flat cuboid reference specimen designated as FLAT state, and two web structures with different widths ($W = 4, 8$ mm) and a height

$H = 6$ mm of the web, designated H6W4 and H6W8, respectively. Technical drawings of the sample geometries are shown in **Figure 1**. The grooves on the left and right sides are required for mounting of the specimens inside the process chamber. After grinding the sample surface to provide equal laser beam absorption, the samples were heat treated, in addition, at 510 °C for 90 min in an inert gas atmosphere. This results in a quasi-stress-free sample state with a surface residual stress of approximately $\sigma_y = -70 \pm 30$ MPa. The initial base material hardness was determined by Martens hardness analysis[18] to a value of HM0.1 = 3850 ± 60 N mm^{-2}. The samples were laser hardened using a 4 kW HPDL of type LDM 4000-100 ($\lambda = 1020$ nm) from Laserline GmbH, Mühlheim-Kärlich, Germany. The average laser power to keep the temperature of 950 °C at the surface along the process path is about $30 \pm 2\%$ of the nominal laser power ($\approx 1.2 \pm 0.08$ kW) for the three specimen geometries. A fiber-coupled laser optics with a nominal diameter of Ø5.8 mm in combination with an inline single color pyrometer was used to harden laser tracks under control of the maximum surface temperature at 950 °C. A pivotable laser optics holder in combination with a linear motor allows for a constant laser beam feed, which was set to 800 mm min^{-1}. The deliberately designed process chamber allows for the control of a He inert gas atmosphere to prevent oxidization of the samples during the laser surface hardening treatment. For the web structures, tracks with a length of ≈ 30 mm (web length, cf. Figure 1) and for the flat specimen, a laser track with a length of about 48 mm were hardened along the x-axis (red arrows). Images of the installed experimental setup at beamline P05 at DESY (Hamburg, Germany), which was used for the in situ synchrotron X-ray diffraction studies, are shown in **Figure 2**.

2.2. In situ X-Ray Diffraction Setup

A scheme of the complete setup for the in situ X-ray diffraction laser surface hardening experiment is shown in **Figure 3**. The

Table 1. Chemical composition of AISI 4140.

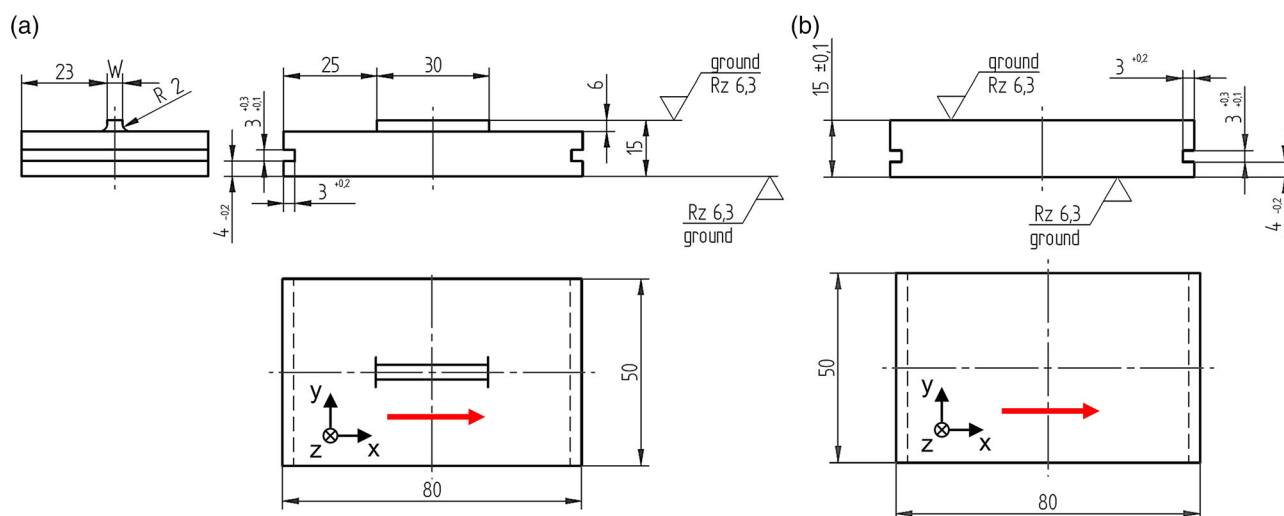| C	Si	Mn	Cr	Mo	S	P	Fe
0.43	0.29	0.73	1.00	0.02	0.06	0.02	bal.

Figure 1. Technical drawings of the investigated sample geometries: a) web structures with height $H = 6$ mm and width $W = 4$ and 8 mm and b) flat sample gemometry (FLAT). Red arrows indicate the laser beam direction. All dimensions are given in mm.
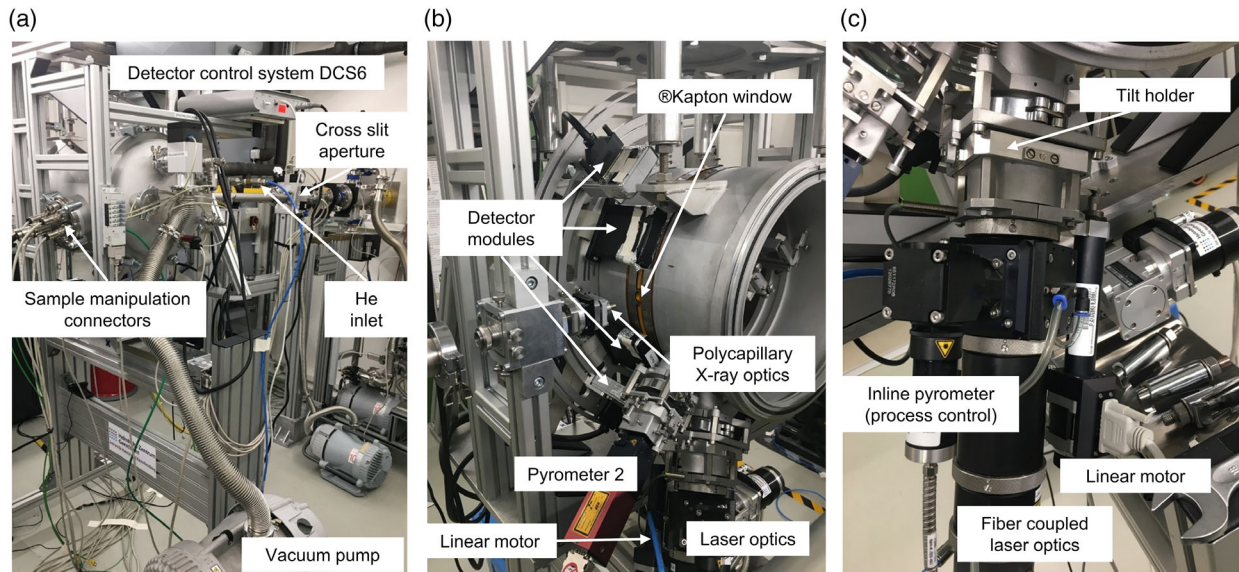
Figure 2. Images of the specially designed process chamber. a) Process chamber connectors and detector control system DCS6, b) detector modules MYTHEN1K, X-ray and optics, and c) Laser optics with linear motor on tilt holder.
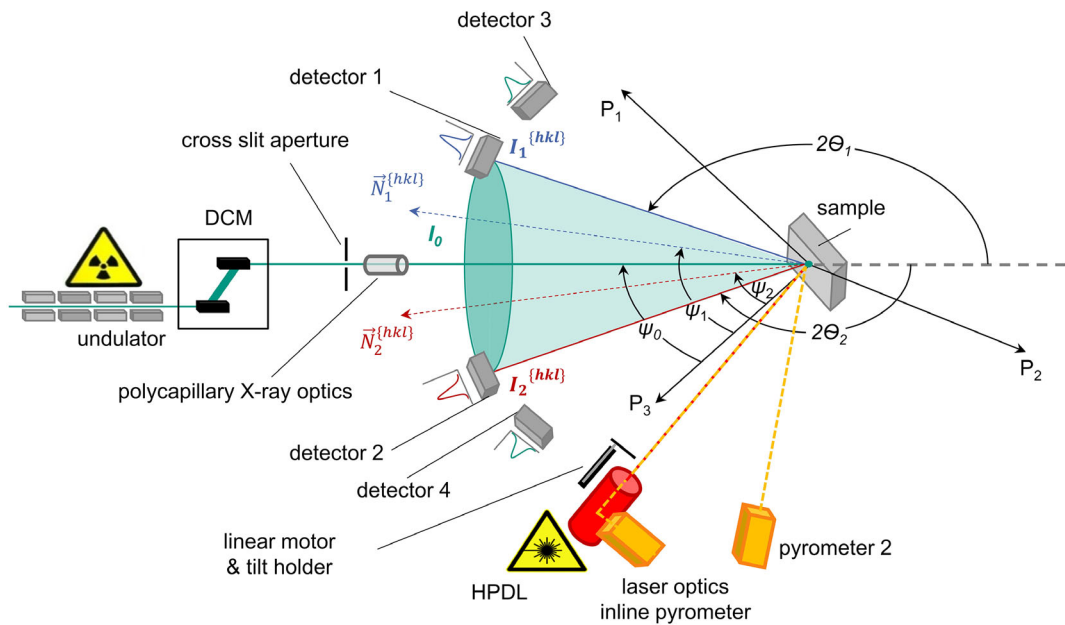

Figure 3. Scheme of the experimental setup for the in situ laser surface hardening experiments.

pairwise (1/2, 3/4), symmetrical arrangement of four fast microstrip line detector modules of type MYTHEN 1K[19] from DECTRIS Ltd., in combination with the pretilted specimen ($\psi_0 = -35°$) allows for the simultaneous recording of a diffraction line $\{hkl\}$ under two different scattering vector orientations $N_1^{hkl} \neq N_2^{hkl}$ or $\psi_1 \neq \psi_2$, respectively, from the identical diffraction cone, according to the single exposure technique, described in the study by Macherauch and Müller.[20] The angular calibration of the detector modules were carried out by illumination of a glass sample for flat field background correction, as well as by use

of iron powder specimen and a LaB6 standard. The synchrotron radiation was set to a photon energy of $E = 10.9\,keV$ ($\lambda = 1.1384\,Å$) using a double crystal monochromator (DCM). For the occurring body-centered phases α/α', the reflections $\{422\}$ and $\{332\}$ and for the face-centered γ phase, the $\{531\}$ and depending on the temperature the $\{442\}$ diffraction lines were recorded partially. The peaks were fitted using a Pseudo-Voigt function and fit errors based on a 95% confidence interval were propagated. Data evaluation according to the $\sin^2 \psi$ method[20] allowed for the time-resolved determination of stresses in the

**ADVANCED
SCIENCE NEWS**

www.advancedsciencenews.com

**ADVANCED
ENGINEERING
MATERIALS**

www.aem-journal.com

surface parallel, transverse (y) direction to the laser track in the center of the process path. In doing so, a measurement frequency of 50 Hz was realized. For stress calculation, diffraction elastic constants (s_1^{hkl}, $\frac{1}{2}s_2^{hkl}$) based on single-crystal elastic constants C_{ij} from the study by Every and McCurdy[21] were utilized, assuming the grain interaction as described by Kröner,[22] whereas the temperature dependency was considered through a temperature factor T_{ij}.[21] The $\{hkl\}$-specific stress values are calculated by Equation (1)

$$\sigma_{\varphi\psi,n}^{hkl} = -\frac{1}{2}\cot(\theta_n^{hkl*}) \cdot \left[\frac{2\theta_{1,n}^{hkl} - 2\theta_{2,n}^{hkl}}{\sin^2(\psi_{1,n}^{hkl}) - \sin^2(\psi_{2,n}^{hkl})}\right] \cdot \frac{1}{2}s_2^{hkl-1}$$

$$= -\frac{1}{2}\cot(\theta_n^{hkl*}) \cdot m_n \cdot \frac{1}{2}s_2^{hkl} - 1 = (\varepsilon_{y,n}^{hkl} - \varepsilon_{z,n}^{hkl}) \cdot \frac{1}{2}s_2^{hkl-1} \tag{1}$$

where the indexes $1(3), 2(4)$ mark the equivalent detector module, n is the sequential number of the illumination, m_n is the slope of the fitted $\sin^2\psi$ line, and θ_n^{hkl*} is the corresponding Bragg angle in the strain-free direction based on the assumption of a plane, rotational symmetric stress state. The determined $\{hkl\}$-specific strains ($\varepsilon_{y,n}^{hkl}$, $\varepsilon_{z,n}^{hkl}$) were averaged analogously to Daymond,[23] and macroscopic stresses (cf. Equation (2)) were determined for visualization purposes.

$$\overline{\sigma}_{\varphi\psi,n} = \sigma_{y,n} = \Delta\overline{\varepsilon}_n \cdot \frac{1}{2}s_2^{\text{mech}-1} \tag{2}$$

2.3. Ex situ Analysis

The postprocess characterizations were divided into laboratory X-ray analyses and metallographical investigations (microhardness tests and optical microscopy), both carried out at KIT. The applied procedures were further detailed in the following two subsections.

2.3.1. X-Ray Lab Analysis

Residual stress analyses were carried out according the $\sin^2\psi$ method[20] using a conventional ψ diffractometer. Thereby, the $\{211\}$ α-iron diffraction line was investigated using V-filtered CrK$_\alpha$ radiation ($2\theta_0 = 156.394°$). High spatial resolution was achieved using Ø100 μm polycapillary optics on the primary beam side by Helmut Fischer GmbH, Sindelfingen, Germany. For each specimen, the transverse surface residual

stresses were analyzed using 15 ψ angles in the range of $-60° \leq \psi \leq +60°$ (equidistant in $\sin^2\psi$). In front of the scintillation detector, a symmetrizing slit according to Wolfstieg[24] was used. For residual stress calculation, the elastic constants $s_1^{hkl} = -1.23 \times 10^{-6}$ MPa^{-1} and $\frac{1}{2}s_2^{hkl} = 5.7 \times 10^{-6}$ MPa^{-1} according to the study by Kröner[22] based on the study by Every and McCurdy[21] were used.

2.3.2. Metallography

For microstructure analyses, cross-sectional specimens were carefully prepared using electric discharge machining (EDM). Afterwards, the specimens were ground, polished, and etched with 2% Nital solution for optical microscopy investigations. In addition, microhardness tests were carried out according to DIN EN ISO 14577[18] using an instrumented microhardness testing system of type Fischerscope H100 from Helmut Fischer GmbH, Sindelfingen, Germany. Martens hardness values were determined for a test load of 100 mN and loading/unloading cycles of 20 s each, using a Vickers indenter. The cross-sectional process zones were fully mapped with an average distance of $\Delta y = 200$ μm and $\Delta z = 50$ μm, respectively.

3. Finite Element Simulation

The finite element (FE) simulation of the laser surface hardening experiments were carried out using the commercial finite elemente software package ABAQUS/CAE by Dassault Systèmes. Therefore, for every sample geometry, 3D models were meshed using hex elements of type (D)C3D8. In **Figure 4**, images of the finite element method (FEM) meshes for the three sample geometries are given. For the web structures full models (cf. Figure 4a,b) were used in the numerical simulation, whereas for the FLAT model (cf. Figure 4c) a semimodel was generated. A general description of the laser hardening simulation approach with the utilized ABAQUS subroutines is given in the study by Kiefer et al.[25] The temperature dependencies of thermal and mechanical properties of the occurring phases are given by a third-order polynomial approach, where the resulting quantities were homogenized according to their phase volume fraction. A precise specification of the input parameters is given in the study by Kaiser et al.[26] First, a purely thermal simulation is carried out for every specimen model, thereby a nodal temperature field is
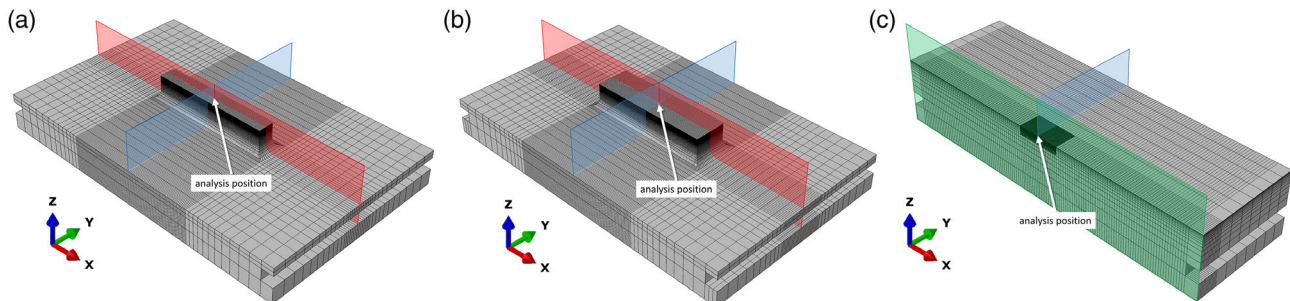

Figure 4. Meshed FEM models of the different specimen geometries. a) Full model of web structure H6W4, b) full model of web structure H6W8, and c) semimodel for the flat (FLAT) geometry with indicated symmetry plane (green). Longitudinal (red) and transverse (blue) cutting planes indicated.

computed. This temperature field serves as input parameter for the subsequent mechanical simulation for stress evaluation.

3.1. Thermal Modeling

During laser surface hardening, high heating and cooling rates of several thousands of $K\,s^{-1}$ occur. Hence, only the phase changes from the initial tempered phase (ferrite) to austenite $\alpha \rightarrow \gamma$ (austenitization) and from austenite to martensite $\gamma \rightarrow \alpha'$ are considered. Additional phase transformations, e.g., bainite formation or carbide precipitation by tempering are not considered in the current FE-model, as only single line experiments without overlapping tracks are investigated. When regarding multiple and overlapping laser tracks, tempering effects might affect the results and the material model has to be extended accordingly. In the following two subsections, the exterior surface fluxes together with the mathematical description of the laser optics and the interior body heat fluxes and a description of the phase transformations is given.

The laser optics tool is realized as a surface flux, which is calculated and implemented in the ABAQUS user subroutine DFLUX. The laser optics intensity distribution was analyzed using a FocusMonitor35 beam diagnosis device from PRIMES GmbH, Pfungstadt, Germany. The intensity distribution I_{Laser} was measured at a fixed laser power of 500 W. The profile, normalized to 1 W, is approximated by an exponential approach and implemented in the simulation according to Equation (3):

$$I_{\text{Laser}} = \frac{1}{500\,\text{W} \times 10^{-2}} \sum_{k=1}^{2} a_k \cdot \exp(b_k \cdot r)\, [\text{W}\,\text{mm}^{-2}] \qquad (3)$$

where a_k and b_k are the fitted coefficients, which are shown in **Table 2** and r is the radius of the laser optics intensity distribution with $\{|r| \in \mathbb{R} : 0 \leq r \leq 3\}$.

A proportional–integral–derivative controller was implemented to control the surface temperature by comparing the specified control temperature $T_{\text{control}}(t)$ and actual temperature $T_{\text{act}}(t)$ in the center of the laser spot, and then adjusting the incremental change of the laser beam power ΔP_{Laser}. Therefore, the incremental change in laser power $\Delta P_{\text{Laser},i}$ is calculated at a rate of 10 ms. In addition, natural convection at the model's outer surfaces is considered toward the surrounding free, static air at room temperature (20 °C). Internal body fluxes and heat as well as phase transformations are considered in the ABAQUS user subroutine UMATHT, based on uncoupled heat transfer calculations. The homogenized, temperature- and phase-dependent parameters are used to solve Fourier's equation to determine the temperature distribution in the workpiece for each timestep:

$$\rho C_{\text{p,hom}} \frac{dT}{dt} + H = \nabla(\lambda_{\text{H,hom}} \nabla T) \qquad (4)$$

Table 2. Coefficients of the approximated laser optics beam profile.

k	1	2
a_k	−4.007	2207.0
b_k	2.006	−0.07336

where ρ is the density, $C_{\text{p,hom}}$ is the homogenized heat capacity, H is the latent heat due to phase transformation, $\lambda_{\text{H,hom}}$ is the homogenized heat conductivity, and T is the temperature at the integration point. Simultaneously with the temperature modeling, the equations describing phase kinetics are solved. The diffusion controlled austenitization is modeled by a modified Johnson–Mehl–Avrami–Kolmogorov (JMAK)[27] approach, as proposed by Miokovic for high heating rates.[28]

The diffusionless martensitic hardening is implemented as proposed by Koistinen and Marburger.[29]

3.2. Mechanical Modeling

The total increment of the strain tensor is summarized by

$$d\varepsilon_{ij}^{\text{tot}} = d\varepsilon_{ij}^{\text{th}} + d\varepsilon_{ij}^{\text{el}} + d\varepsilon_{ij}^{\text{pl}} + d\varepsilon_{ij}^{\text{pt}} + d\varepsilon_{ij}^{\text{tp}} \qquad (5)$$

The thermally induced strain increments ($d\varepsilon_{ij}^{th}, d\varepsilon_{ij}^{pt}, d\varepsilon_{ij}^{tp}$) are determined in the ABAQUS user subroutine UEXPAN. Whereby the purely thermal strains ($d\varepsilon_{ij}^{th}$) are calculated for each phase fraction with the temperature-dependent coefficient of thermal expansion. Strain changes due to phase transformations ($\Delta\varepsilon_{ij}^{pt}$) are also considered according their incremental phase fraction df_p, where p describes the formed phase. The anisotropic change of transformation-induced plastic strains $d\varepsilon_{ij}^{tp}$ are described based on Greenwood and Johnson,[30] further developed by Leblond et al.[31] The purely mechanical strain changes ($d\varepsilon_{ij}^{el}$ and $d\varepsilon_{ij}^{pl}$) are calculated in the ABAQUS user subroutine UMAT according to Hooke's law with phase and temperature homogenized properties, and the plastic strain parts using a Newton algorithm and forwarded into an hardening approach as proposed by Voce[32] given by the expression

$$\sigma_{\text{yield}} = \sigma_0 + R_0 \varepsilon_{\text{pl}} + R_1(1 - \exp(-e\varepsilon_{\text{pl}})) \qquad (6)$$

where σ_0, R_0, R_1, and e are fit parameters. A detailed description of the mechanical modeling and determination of the fit parameters is also given by Kaiser et al.[26]

4. Results and Discussion

In **Figure 5**, cross-sectional micrographs, after metallographic preparation, are shown for each specimen geometry. The brighter regions in the micrographs depict the martensitic hardened process zones with a sharp transition area at the edges to the darker unaffected base material. The mentioned transition zone has, in all cases, a width of about 50 μm. It can be seen clearly, that the process zone width w and depth d are slightly larger for the web geometries in contrast to the flat sample (cf. Figure 5c) and largest for the smaller web structure H6W4. This observation can be explained by a heat build-up in the webs based on the decreased heat conduction into the surrounding material and, subsequently, a wider and deeper material region will form austenite and transform into martensite. In addition, in Figure 5a, for H6W4, it is observed that the process zone is asymmetrical from left to right, in contrast to the hardening lenses for H6W8 and the FLAT specimen. This is due to the non perpendicular laser irradiation in the in situ experiment.
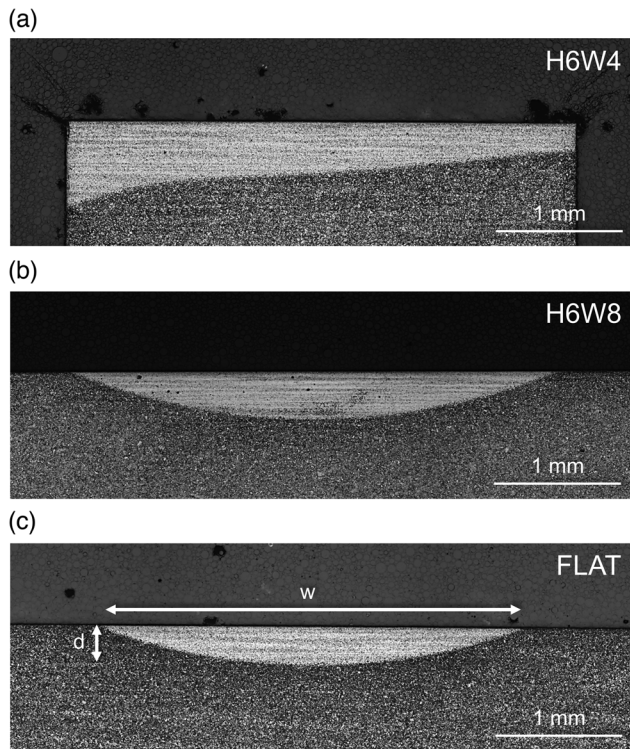
**ADVANCED
SCIENCE NEWS**

www.advancedsciencenews.com

**ADVANCED
ENGINEERING
MATERIALS**

www.aem-journal.com

(a)

H6W4

1 mm

(b)

H6W8

1 mm

(c)

FLAT

w

d

1 mm

Figure 5. Cross-sectional micrographs for the specimens: a) H6W4, b) H6W8, and c) FLAT, where process zone center depth d and surface width w are indicated.

In the case of H6W8 and FLAT, the behavior is compensated by the sufficiently large, flat, irradiated area (web width W). The associated results from the Martens hardness tests are shown in **Figure 6** as contourplots. All samples show a similar hardness values, with process zone hardness averaged over all samples of approximately $HM0.1 = 6610 \pm 160 \, N \, mm^{-2}$. The determined process zone dimensions are in good agreement with the microscopy analyses. The process zones appear to be slightly smaller than the microscopical images, which is attributed to the coarse measurement grid for the hardness tests.

Figure 7 shows the martensite content in cross-sectional views, cut along the blue shaded planes (cf. Figure 4), for the three investigated geometries in the final state. For visualization purposes, the results of the FLAT geometry are duplicated and mirrored along the y-axis. The simulation qualitatively predicts the process zone dimensions correctly. On a quantitative scale, there is a slight overestimation of the process zone depth of about $+50 \, \mu m$. Interpolation of the color coding causes the misleading rendering of a larger transition zone. This is affected by the element size of the mesh.

In **Figure 8**, a comparable view is given by means of a 2D contourplot for the distribution of the transverse stress component σ_y over the cross-sectional area after laser surface hardening. For presentation reasons, the color coding of the stresses is not identical for the three geometries, as the absolute residual stress values for the three geometries differ strongly. In all cases, it is observed, that compressive residual stresses (blue) are formed inside the process zone, which are locally compensated

by high tensile residual stresses (red) further below. The global distribution of samples H6W8 and FLAT appear similar. Compressive residual stresses exist inside the process zone. The regions with high compressive, rather homogeneous residual stresses are lenticular on the cross-sectional view and coincide well with the martensitic hardened regions presented in Figure 7. This region with high compressive residual stresses is surrounded by a zone with balancing tensile residual stresses. The contourplots indicate that the maximum balancing tensile residual stress is below the center of the processed area, adjacent to the process zone. The maximum in tensile residual stresses is about 1070 and 810 MPa for the FLAT and H6W8 samples, respectively. However, near the surface, toward the edges of the process zone, a slight increase in compressive residual stresses can be observed for both samples (Figure 8b,c). The maximum compressive residual stresses in these regions amount to about -580 and -530 MPa for the samples H6W8 and FLAT, respectively. For all three cases investigated here, approximately the same amount of compressive residual stresses transverse to the laser track were determined in the near surface region of the center of the process zone, with a value of about -310 ± 30 MPa (see also **Figure 9** in the final state, right). Regarding the residual stress distributions σ_y for samples FLAT and H6W8, it can be observed that, regardless of the different color codings, the region exhibiting compressive residual stresses are extending further in case of the web structure H6W8, compared with the FLAT geometry. However, the region exhibiting balancing tensile residual stresses appears to be smaller. This, as well as the differences in the maximum tensile residual stresses, according to the indications shown earlier, can be explained by the difference in constraints between the FLAT sample and the web structure, i.e., in case of the web structure, the available material volume is insufficient to generate a corresponding build-up of residual stress. Furthermore, the web structures cause changes in the triaxial residual stress distribution in the process zone and the adjacent regions. This situation alters the resulting residual stress distributions in transverse direction, when regarding the more narrow web structure H6W4. Here, the region with compressive residual stresses is slightly tilted, similar to the martensitic hardened zone, as shown in Figure 7a. A further difference to the samples H6W8 and FLAT is the less homogeneous compressive residual stress distribution. In contrast to the other two samples, the compressive residual stresses close to the surface do not increase toward the edges of the laser-processed zone, which coincides with the web edges in this case. Instead the compressive residual stresses continuously decrease toward the sample edges, where they amount to 0 MPa. Regardless of the color coding, the dimensions of the balancing tensile residual stress region is even smaller. The maximum tensile residual stresses underneath reach from about 490 MPa for H6W4 to the maximum compressive residual stress value of ≈ -300 MPa at the surface in the center of the process zone.

In Figure 9, the experimentally determined temporal transverse surface stress courses σ_y inside the process zone center for all three specimen geometries are shown together with the corresponding courses at the analysis positions, cf. Figure 4, determined by numerical process simulations (red lines). In addition, for each specimen, the residual stress values determined by means of ex situ analyses in the surface center of
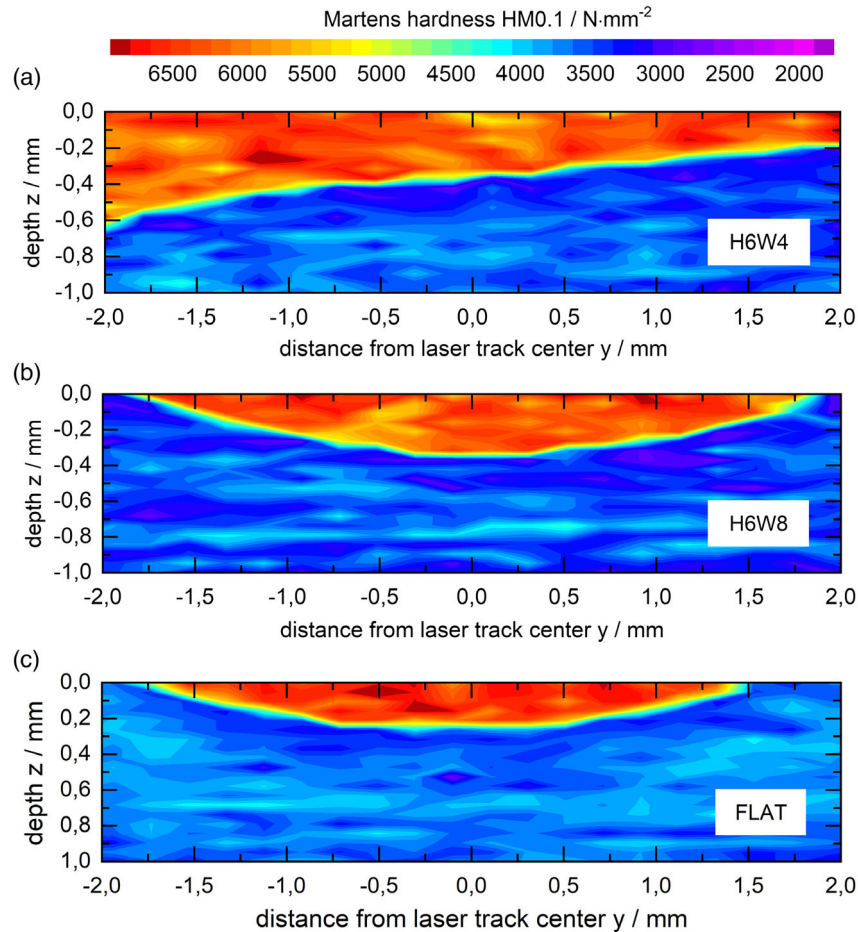
ADVANCED
SCIENCE NEWS
www.advancedsciencenews.com

ADVANCED
ENGINEERING
MATERIALS
www.aem-journal.com

Figure 6. Contourplots based on Martens hardness tests on the cross sections for the samples: a) H6W4, b) H6W8, and c) FLAT.

the process zone are given at the right side of the diagrams (unfilled squares). In all diagrams shown here, three points in time are specified based on the results from the simulated stress evolution, from left to right t_1 at the compressive stress maximum, t_2 at the tensile stress maximum, and t_3 for the final state after laser hardening. All courses are similar in the beginning, where the stresses at the measurement position have their initial residual stress value. With the laser beam approaching, the compressive residual stresses are reduced, and in case of H6W8 and FLAT transformed to a first tensile stress maximum. A steep temperature rise, due to the approaching laser beam, leads to high thermal strains in the center of the process zone, which are constraint by the surrounding, cooler material where, e.g., for H6W4, the transverse thermal expansion of the material is less inhibited than for the other specimen geometries. This results in a first compressive stress maximum at t_1. The level of the compressive stress maximum is determined by the amount of constraints, therefore lower for H6W4 ($\sigma_y = -430\,\text{MPa}$) and increasing toward FLAT ($\sigma_y = -550\,\text{MPa}$). This geometry effect was previously observed for specimen geometries with radii in the study by Kiefer et al.[17] With a further temperature increase, the warm yield strength decreases and the compressive stresses decrease due to plastic deformation. The reduction of compressive stresses toward 0 MPa is further supported by the $\alpha \rightarrow \gamma$ phase transformation and the corresponding volume contraction inside the process zone. After reaching the surface maximum temperature at the measurement position, the stress course changes the sign to tensile stresses, which is explained by the thermal contraction during cooling down, due to the higher coefficient of thermal expansion of austenite (γ) in contrast to ferrite (α). A further temperature decrease leads to an increase in the tensile stress σ_y toward a maximum at t_2 with $\approx 160\,\text{MPa}$ for H6W4, 220 MPa for H6W8, and 260 MPa for FLAT. The height of this tensile stress maximum is associated with the amount of constraints, as mentioned earlier for the discussion of the compressive stress maximum. From the expanse of the austenite regime (green shaded area), as well as from the time period until the transverse tensile stress maximum is reached, a heat build-up in the webs (H6W4, H6W8) delays martensite formation, in comparison witht the FLAT sample. Comparing the two webs (cf. Figure 9a,b) allows for the conclusion, that the austenite period is inversely proportional to the web width W and the length is doubled with halving of the width and vice versa. So far, deviations between experimentally determined stress courses and the results of the FE simulation occur, especially for the web
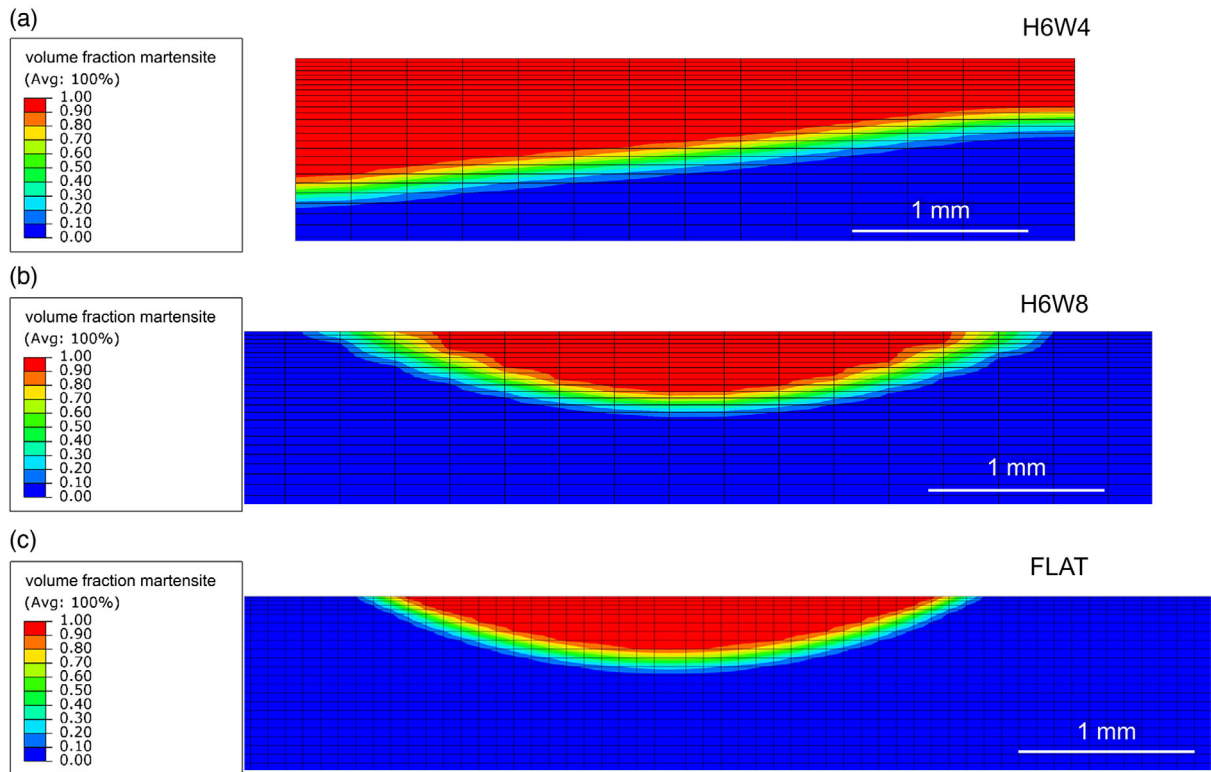
ADVANCED
SCIENCE NEWS

www.advancedsciencenews.com

ADVANCED
ENGINEERING
MATERIALS

www.aem-journal.com

Figure 7. Cross-sectional martensite phase fraction from the numerical simulation for the specimens: a) H6W4, b) H6W8, and c) FLAT.
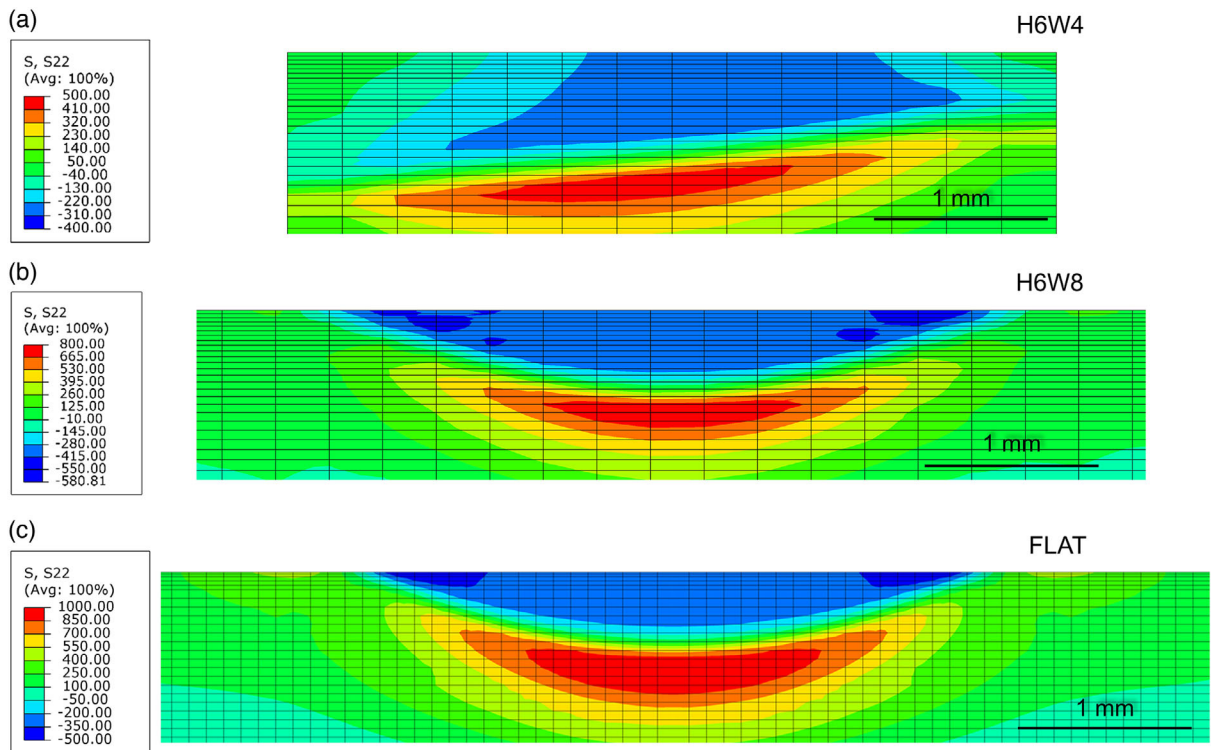

Figure 8. Cross-sectional residual stress distributions σ_y from the numerical simulation for the specimens: a) H6W4, b) H6W8, and c) FLAT.

**ADVANCED
SCIENCE NEWS**

www.advancedsciencenews.com

**ADVANCED
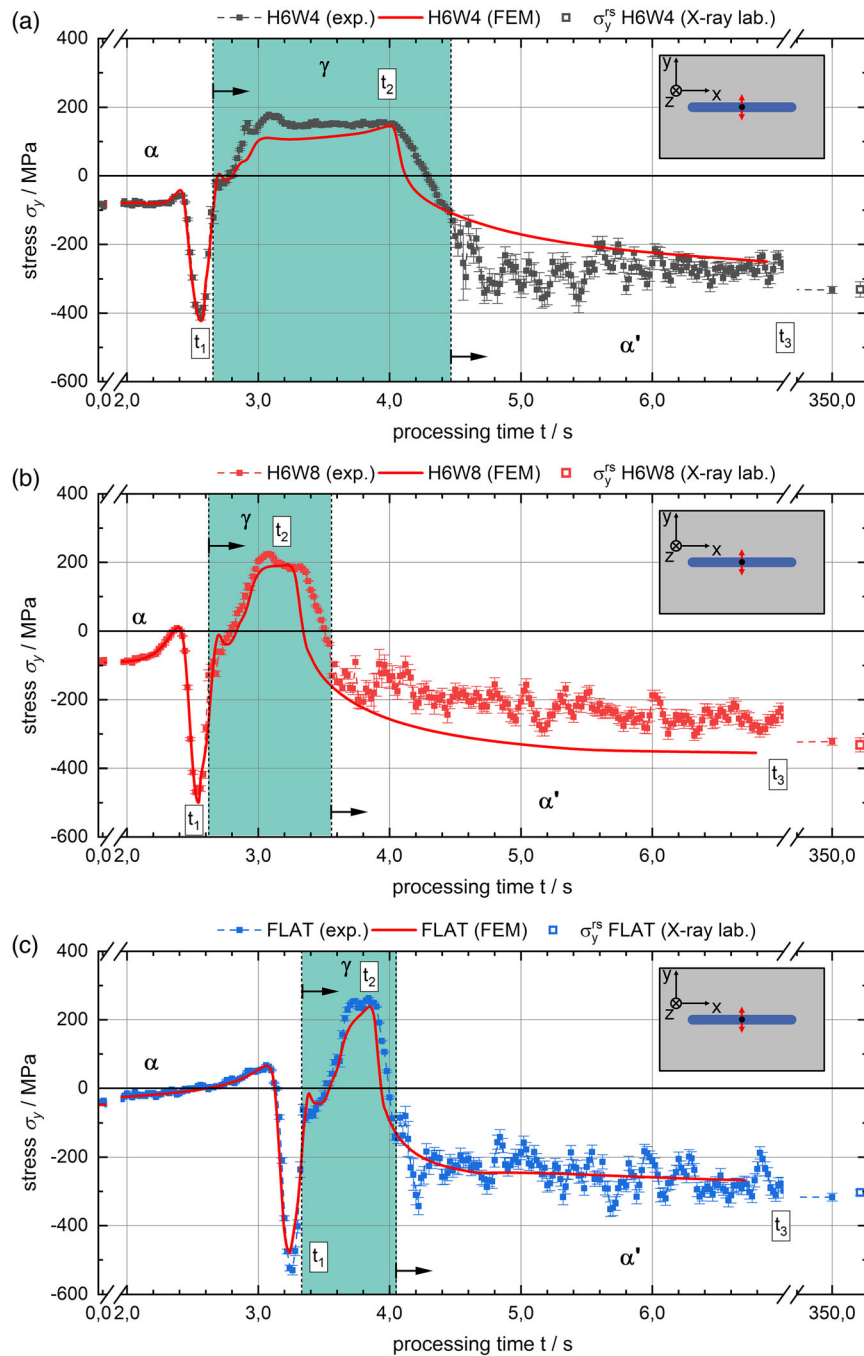ENGINEERING
MATERIALS**

www.aem-journal.com

Figure 9. In situ surface stress courses σ_y transverse to the laser track together with the corresponding results from the FEM simulations and the correpsonding residual stresses in the center of the process zone, determined in the X-ray lab for the a) H6W4 geometry, b) H6W8 geometry, and c) the FLAT specimen. Phase transitions indicated by right arrows (austenite regime is shaded green) regions also phase regions are marked (α, γ, α').

structures. A reason might be the coarser mesh for the full web models compared to the FLAT semi model, cf. Figure 4. Mesh sizes were chosen to keep computation time sufficiently low. After the tensile stress maximum, with further cooling, the transverse stress decreases, changes sign, and becomes compressive stress again. This decrease is explained by the previous formation of martensite at the edges of the process zone associated with a volume expansion and thus reducing the tensile stresses. While

reaching the martensite start temperature M_s, the local volume expansion is accompanied by an additional, slight increase in compressive stresses toward t_3, which is approximately on the level of the ex situ determined residual stresses for all cases. Observed deviations for H6W8 in Figure 9b are considered low and are so far not explicable. However, they might be attributed to the mesh quality as well. Improving the mesh quality would result a finer mesh grid and thus a significantly increased
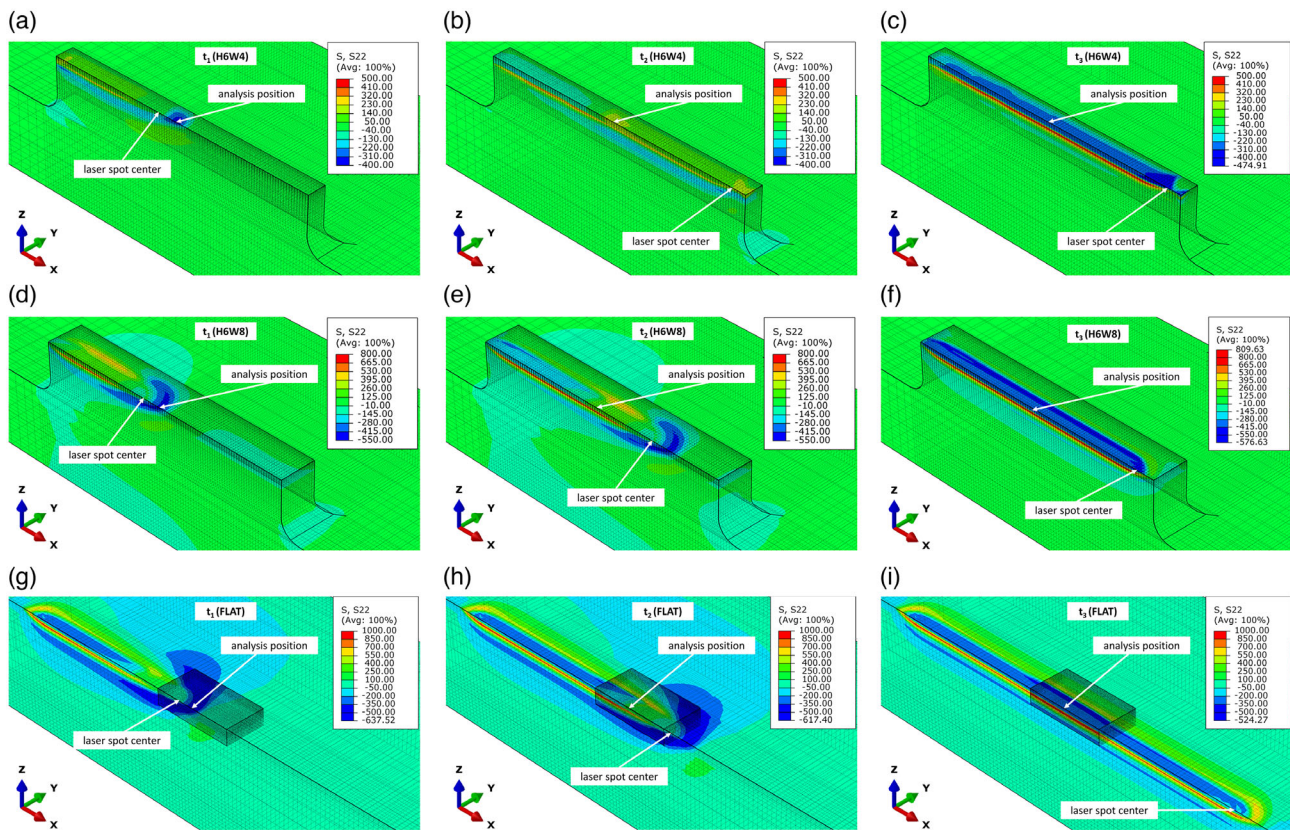
**ADVANCED
SCIENCE NEWS**

www.advancedsciencenews.com

**ADVANCED
ENGINEERING
MATERIALS**

www.aem-journal.com

Figure 10. Transverse stress σ_y distributions in cut views (along red planes, cf. Figure 3) for the three points in time t_1, t_2, and t_3 from FEM for a–c) the web specimen H6W4, d–f) the web specimen H6W8, and g–i) the FLAT specimen.

number of elements in the model. This would prolong the simulation time disproportionately to the gain in accuracy. In **Figure 10**, sectional views along the red marked planes (cf. Figure 4a,b) and the green marked symmetry plane (cf. Figure 4c) are shown for the 3D distribution of the transverse stress component σ_y for all three specimen geometries as well as the three points in time t_1, t_2, and t_3. At t_1 it is observed that a larger, more pronounced compressive stress region for the FLAT geometry surrounds the laser irradiated area on the surface as well as in depth. This characteristic is decreasing with smaller web geometry. The stress distribution at t_2 for H6W4 shows only small transverse stresses along the web in contrast to H6W8 and FLAT. As mentioned earlier, lower cooling through a decreased heat sink effect causes a delayed martensite formation. For the discussion of local differences between the geometry variants, the positions of the laser beam, at the three points in time are indicated. Regarding this additional information, it can be observed, that for t_2 large deviations exist. The laser spot in Figure 10b is already at the end position, whereas for the other geometries, depending on the heat sink effect provided through the geometry, the laser beam is only just ahead of the measurement or analysis position in the center of the web. For this point in time, the transient stress evolution is strongly affected by heat dissipation and the heat sink effect in combination with the difference in local constraints. Ahead of the zone currently irradiated by the laser beam, a region with rather high compressive

stresses is formed. Behind the current laser beam position, where the material is already cooling down, tensile stresses occur. This region is larger with smaller web geometry, cf. Figure 10b,e,h. In the course of temperature balancing, in particular in the course of the martensitic transformation, homogeneous compressive stresses are formed (see also t_3). However, this transition is heavily influenced by local heat dissipation and local constraints as in the final state (see also Figure 8 for the resulting residual stress distributions). In comparison with the time-dependent stress evolution shown in Figure 9, it can be clearly seen that the surrounding stress distribution strongly affects the local stress evolution in the center of the process zone. For the last point in time t_3 (cf. Figure 10c,f,i), a full blue line denotes the field of compressive residual stresses at the surface with a depth extension, as shown in Figure 8. In this final state, high transverse tensile stresses surrounding the start and end position of the laser track at the surface of the FLAT geometry are observed, in contrast to the web geometries. In the application of laser hardening a workpiece, geometric features might affect the fatigue properties positively, as at the surfaces where fatigue cracking is initiated, fewer unfavorable tensile residual stress states are formed.

In summary, the experimentally determined transverse stresses at process end are in very good agreement with the results of conventional (laboratory based) X-ray residual stress analyses. Furthermore, temporally and spatially resolved

transverse surface stress prediction by numerical simulation is possible on a quantitative scale with satisfying quantitative deviations ($\approx 10\%$ for σ_y^{rs}) for the investigated states. The most accurate process prediction was achieved for the sample FLAT (cf. Figure 9c). Hence, the current FE process simulation yields the advantage of time resolved depth information, allowing deeper insights into the stress evolution during laser surface hardening. These results cannot be provided through experimental approaches. It was demonstrated that the simulation approach can be transferred to more complex surface geometries, as illustrated in this work for two different web structures.

Additional experimental in situ datasets now allow for the ongoing improvement of the simulation tool to improve process predictions on a broader parametric range, as e.g., control temperature, laser power, and laser feed velocity or the application of the laser treatment to further workpiece materials.

5. Conclusion

Three different specimen geometries made of AISI 4140 were laser surface line hardened under control of the surface temperature (950 °C) with a laser velocity of 800 mm min^{-1}. Thereby, in situ stress evolutions were determined with a measuring frequency of 50 Hz, using a unique experimental setup for synchrotron X-ray diffraction during laser surface line hardening. In addition, corresponding numerical process simulation of laser surface line hardening were carried out using the commercial FE modeling package ABAQUS/CAE. From the presented experimental and numerical results the following general conclusions can be drawn: i) The presented simulation tool provides numerical predictions of laser surface line hardening of complex surface structures on a quantitative scale. The temporally and spatially resolved simulation data allow for deeper insights into the stress evolution during laser surface hardening due to the access to time-resolved 3D information. ii) The transverse surface stress courses, predicted by the simulation for all three geometries considered here, are in very good agreement with results from elaborate experimental in situ X-ray diffraction analyses. iii) Only on basis of the temporal evolution of 3D stress distributions, which can be provided exclusively by a comprehensive process simulation, is a proper evaluation of laser surface line hardening possible for more complex shaped surface geometries, as presented here for various web structures.

With regard to the presented process variations we can further conclude that: iv) A significant difference in the temporal stress evolution for the three investigated geometries exist in particular in the region of supercooled austenite, where, in all cases, a tensile stress plateau occurs, which is significantly wider with smaller web geometry according to the higher heat accumulation in the webs. v) A heat build-up in the web, through hindered heat conduction, leads to a more expansive hardening width w and depth d, however, the absolute hardness increase is not affected. vi) Local residual stresses are extremely dependent on the local geometry. The narrower the web structure, the more inhomogeneous the local compressive residual stress distribution in the process zone. The reason for this is a) to be found in the local heat dissipation and b) in the locally present fewer constraints in case of narrow web structures. vii) Higher compensating tensile residual stresses occur for the flat specimen compared to the web structures, which again is due to the change in heat dissipation and constraints. viii) The surface residual stresses, in particular, in the center of the process zone, are independent of the web geometry for the investigated specimens.

Conflict of Interest

The authors declare no conflict of interest.

Data Availability Statement

Research data are not shared.

[1] DIN 17022-5:2000-03, *Wärmebehandlung von Eisenwerkstoffen – Verfahren der Wärmebehandlung – Teil 5: Randschichthärten*, Beuth-Verlag, Berlin **2000**.

[2] F. Bachmann, *Appl. Surf. Sci.* **2003**, *208–209*, 125.

[3] I. Pashby, S. Barnes, B. Bryden, *J. Mater. Process. Technol.* **2003**, *139*, 585.

[4] E. Kennedy, G. Byrne, D. Collins, *J. Mater. Process. Technol.* **2004**, *155–156*, 1855.

[5] J. C. Ion, *Surf. Eng.* **2002**, *18*, 14.

[6] R. S. Lakhkar, Y. C. Shin, M. J. M. Krane, *Mater. Sci. Eng., A* **2008**, *480*, 209.

[7] G. Tani, L. Orazi, A. Fortunato, *CIRP Ann.* **2008**, *57*, 209.

[8] C. Yao, B. Xu, J. Huang, P. Zhang, Y. Wu, *Opt. Lasers Eng.* **2010**, *48*, 20.

[9] E. Liverani, A. H. Lutey, A. Ascari, A. Fortunato, L. Tomesani, *Surf. Coat. Technol.* **2016**, *302*, 100.

[10] F. Cordovilla, Á. García-Beltrán, P. Sancho, J. Domínguez, L. Ruiz-de Lara, J. L. Ocaña, *Mater. Des.* **2016**, *102*, 225.

[11] P. De la Cruz, M. Odén, T. Ericsson, *Int. J. Fatigue* **1998**, *20*, 389.

[12] K. Müller, C. Körner, H. Bergmann, *Härterei-Tech. Mitt.* **1996**, *51*, 19.

[13] N. S. Bailey, W. Tan, Y. C. Shin, *Surf. Coat. Technol.* **2009**, *203*, 2003.

[14] V. Kostov, J. Gibmeier, F. Wilde, P. Staron, R. Rössler, A. Wanner, *Rev. Sci. Instrum.* **2012**, *83*, 115101.

[15] D. Kiefer, J. Gibmeier, F. Beckmann, F. Wilde, *Residual Stress*, Materials Research Forum LLC, Vol. 2, **2017**, pp. 467–472.

[16] D. Kiefer, J. Gibmeier, F. Beckmann, *Mechanical Stress Evaluation by Neutron and Synchrotron Radiation*, Materials Research Forum LLC, Vol. *4*, **2018**, pp. 91–96.

[17] D. Kiefer, J. Gibmeier, F. Wilde, F. Beckmann, *Minerals, Metals, and Materials Series*, Springer **2020**, pp. 2127–2138.

[18] *DIN EN ISO 14577-1:2015-11, Metallische Werkstoffe – Instrumentierte Eindringprüfung zur Bestimmung der Härte und anderer Werkstoffparameter – Teil 1: Prüfverfahren (ISO 14577-1:2015); Deutsche Fassung EN ISO 14577-1:2015*, Beuth-Verlag, Berlin **2015**.

[19] B. Schmitt, C. Brönnimann, E. F. Eikenberry, F. Gozzo, C. Hörmann, R. Horisberger, B. Patterson, *Nucl. Instruments Methods Phys. Res. Sect. A Accel. Spectrometers, Detect. Assoc. Equip.*, Vol. *501*, North-Holland **2003**, pp. 267–272.

[20] E. Macherauch, P. Müller, *Z. Angew. Phys.* **1961**, *13*, 305.

[21] A. G. Every, A. K. McCurdy, *Second High. Order Elastic Constants*, Springer-Verlag **2005**, pp. 11–17.

[22] E. Kröner, *Z. Phys.* **1958**, *151*, 504.

[23] M. R. Daymond, *J. Appl. Phys.* **2004**, *96*, 4263.

[24] U. Wolfstieg, *HTM – J. Heat Treat. Mater.* **1976**, *31*, 24.

[25] D. Kiefer, P. Schüssler, F. Mühl, J. Gibmeier, *HTM – J. Heat Treat. Mater.* **2019**, *74*, 23.

[26] D. Kaiser, J. Damon, F. Mühl, B. de Graaff, D. Kiefer, S. Dietrich, V. Schulze, *J. Mater. Process. Technol.* **2020**, *279*, 116485.

[27] M. Avrami, *J. Chem. Phys.* **1939**, *7*, 1103.

[28] T. Mioković, *Dissertation*, Univeriät Karlsruhe (TU) **2005**.

[29] D. Koistinen, R. Marburger, *Acta Metall.* **1959**, *7*, 59.

[30] G. W. Greenwood, R. Johnson, *Proc. R. Soc. London. Ser. A Math. Phys. Sci.* **1965**, *283*, 403.

[31] J. Leblond, J. Devaux, J. Devaux, *Int. J. Plast.* **1989**, *5*, 551.

[32] E. Voce, *J. Inst. Met.* **1948**, *74*, 537.